

# A Kinematic Link between Boxy Bulges, Stellar Bars, and Nuclear Activity in NGC 3079 & NGC 4388

S. Veilleux<sup>1,2,3</sup>, J. Bland-Hawthorn<sup>3,4</sup>, and G. Cecil<sup>5</sup>

## ABSTRACT

We present direct kinematic evidence for bar streaming motions in two active galaxies with boxy stellar bulges. The Hawaii Imaging Fabry-Perot Interferometer was used on the Canada-France-Hawaii 3.6-m telescope and the University of Hawaii 2.2-m telescope to derive the two-dimensional velocity field of the line-emitting gas in the disks of the Sc galaxy NGC 3079 and the Sb galaxy NGC 4388. In contrast to previous work based on long-slit data, the detection of the bar potential from the Fabry-Perot data does not rely on the existence of inner Lindblad resonances or strong bar-induced shocks. Simple kinematic models which approximate the intrinsic gas orbits as nonintersecting, inclined elliptical annuli that conserve angular momentum characterize the observed velocity fields. In NGC 3079, bar streaming motions with moderately eccentric orbits ( $e = b/a \sim 0.7$ ) aligned along  $PA = 130^\circ$  intrinsic to the disk ( $PA = 97^\circ$  on the sky) are detected out to  $R_b = 3.6$  kpc. The orbits become increasingly circular beyond that radius ( $e = 1$  at  $R_d \approx 6$  kpc). The best model for NGC 4388 includes highly eccentric orbits ( $e \sim 0.3$ ) for  $R_b \lesssim 1.5$  kpc which are aligned along  $PA = 135^\circ$  intrinsic to the disk ( $PA = 100^\circ$  on the sky). The observed “spiral arms” are produced by having the orbits become increasingly circular from the ends of the bar to the edge of the disk ( $R_d \approx 5$  kpc), and the intrinsic bar PA shifting from  $135^\circ$  to  $90^\circ$ .

Box-shaped bulges in both NGC 3079 and NGC 4388 are confirmed using new near-infrared images to reduce dust obscuration. Morphological analysis of starlight in these galaxies is combined with the gas kinematics derived from the Fabry-Perot spectra to test evolutionary models of stellar bars that involve transitory boxy bulges, and to quantify the importance of such bars in fueling active nuclei. Our data support the evolutionary bar models, but fail to prove convincingly that the stellar bars in NGC 3079 and NGC 4388 directly trigger or sustain the nuclear activity.

---

<sup>1</sup>Department of Astronomy, University of Maryland, College Park, MD 20742; E-mail: veilleux@astro.umd.edu

<sup>2</sup>Cottrell Scholar of the Research Corporation

<sup>3</sup>Visiting Astronomers, Canada-France-Hawaii Telescope, operated by the National Research Council of Canada, the Centre de la Recherche Scientifique de France, and the University of Hawaii

<sup>4</sup>Anglo-Australian Observatory, P.O. Box 296, Epping, NSW 2121, Australia; E-mail: jbh@aaopep2.aao.gov.au

<sup>5</sup>SOAR/NOAO, 950 N. Cherry Ave., Tucson, AZ 85726-6732; email: gcecil@noao.edu

*Subject headings:* galaxies: active – galaxies: evolution – galaxies: individual (NGC 3079 and NGC 4388) – galaxies: kinematics and dynamics – galaxies: spiral – galaxies : structure

## 1. Introduction

The origin of galaxy nuclear activity<sup>6</sup> is of fundamental astrophysical importance. Recent surveys suggest that a nonaxisymmetric component to the gravitational potential is necessary to start nuclear activity (e.g., Moles, Márquez, & Pérez 1995). Evidence has mounted that galaxy interactions trigger activity in high-luminosity galaxies (e.g., Sanders & Mirabel 1996; Bahcall et al. 1997; Stockton 1998). However, the evidence is less convincing in lower luminosity, interacting spiral galaxies. These are known to have higher star formation rates on the average than isolated galaxies (e.g., Kennicutt & Keel 1987; Keel & van Soest 1992), but the role of galaxy interactions in triggering nuclear activity in Seyfert galaxies is debated vigorously (e.g., Dahari 1984; Fuentes-Williams & Stocke 1988; Dultzin-Hacyan 1998; De Robertis, Yee, & Hayhoe 1998).

In low-luminosity active galaxies stellar bars may funnel gas down to the scale of the central engine. Observations (e.g., Quillen et al. 1995; Benedict, Smith, & Kenney 1996; Regan, Vogel, & Teuben 1997) and numerical simulations (e.g., Athanassoula 1992; Friedli & Benz 1993, 1995; Piner, Stone, & Teuben 1995) have shown that stellar bars can induce mass inflow at rates sufficient to fuel kpc-scale starbursts ( $\gtrsim 1 M_{\odot} \text{ yr}^{-1}$ ). These results are consistent with the statistical excess of barred galaxies among starbursts (Hawarden et al. 1986; Dressel 1988; Arsenault 1989; Martin 1995; Ho 1996; Huang et al. 1996; see Pompea & Rieke 1990 and Isobe & Feigelson 1992, however). It is unclear how these significant inflow rates can be sustained down to the nuclear scale to feed the AGN, but simulations of “bars within bars” (Norman & Silk 1983; Shlosman, Frank, & Begelman 1989; Wada & Habe 1992; Friedli & Martinet 1993; Heller & Shlosman 1994; Maciejewski & Sparke 1997) and the detections of nested bars (Shaw et al. 1995; Wozniak et al. 1995; Friedli et al. 1996; Erwin & Sparke 1998) and “nuclear mini-spirals” (e.g., Ford et al. 1994; Regan & Mulchaey 1999; Martini & Pogge 1999) are promising developments.

Despite these efforts, it is surprising to find little or no observational evidence for Seyfert nuclei to occur preferentially in barred systems (e.g., McLeod & Rieke 1995; Heraudeau et al. 1996; Mulchaey & Regan 1997) or for emission-line strengths of AGNs to depend on the presence of a bar (Ho, Filippenko, & Sargent 1997). Perhaps nuclear activity in unbarred galaxies was triggered by short-lived bars that have since disappeared. Indeed, evolutionary models of disk

---

<sup>6</sup>In this paper, ‘nuclear activity’ refers to either starburst or black-hole driven activity in the nuclei of galaxies. Similarly, we refer to ‘active galaxies’ as galaxies powered by star formation (starburst galaxies) or through accretion onto a massive black hole (active galactic nuclei or quasars).

galaxies suggest that stellar bars are transient features that form and dissolve over only a few orbital periods (e.g., Hohl & Zang 1979; Miller & Smith 1979; Combes & Sanders 1981; Combes et al. 1990; Pfenniger & Friedli 1991; Raha et al. 1991; Merritt & Sellwood 1994; Norman, Sellwood, & Hasan 1996). In these scenarios, a vertical instability in the bar kicks stars above the disk of the galaxy to produce boxy peanut-shaped bulges that eventually settle to become stellar spheroids. Recent kinematic evidence for stellar bars in galaxies with boxy bulges has provided observational support for this scenario (e.g., Bettoni & Galletta 1994; Kuijken & Merrifield 1995; Merrifield & Kuijken 1999; Bureau & Freeman 1999). Secular dynamical evolution has also been invoked to explain correlations between disk and bulge properties (e.g., Courteau, de Jong, & Broeils 1996).

However, these evolutionary scenarios remain virtually untested for active galaxies. *Morphological* evidence for a barred Seyfert galaxy with a boxy peanut-shaped bulge has recently been presented by Quillen et al. (1997). The present paper will discuss the first unambiguous *kinematic* evidence for a bar potential in two active galaxies with boxy bulges. The objects we discuss – the edge-on Sc galaxy NGC 3079 and Sb galaxy NGC 4388 – show clear signs of nuclear activity at most wavelengths. NGC 3079 is host to the most powerful windblown superbubble known (Filippenko & Sargent 1992; Veilleux et al. 1994, hereafter VCBTFS). Infrared and radio measurements of this galaxy suggest a nuclear starburst that coexists with an AGN (e.g., Lawrence et al. 1985; Irwin & Seaquist 1988; Haschick et al. 1990; Irwin & Sofue 1992; Baan & Irwin 1995). The radio morphology and optical/X-ray spectral properties of the nucleus of NGC 4388 clearly point to a powerful AGN (e.g., Stone, Wilson, & Ward 1988; Hummel & Saikia 1991; Kukula et al. 1995; Hanson et al. 1990; Iwasawa et al. 1997; Falcke et al. 1998). A complex of highly ionized line-emitting gas clouds extends several kpc above the galactic plane (e.g., Pogge 1988). The origin of this extraplanar material has been discussed in detail by Veilleux et al. (1999; hereafter VBCTM).

The proximity of NGC 3079 (17.3 Mpc or 84 pc arcsec<sup>-1</sup> based on Tully, Shaya, & Pierce 1992) and NGC 4388 (16.7 Mpc or 81 pc arcsec<sup>-1</sup> based on Yasuda, Fukugita, & Okamura 1997) allows for detailed structural studies. The stellar bulge of NGC 3079 presents a striking box/peanut shape at optical wavelengths (Shaw, Wilkinson, & Carter 1993 and references therein). A stellar bar in NGC 3079 has been posited (e.g., de Vaucouleurs et al. 1991), but such suggestions were often based on the morphology of the central region rather than on the kinematics. To date, the most detailed study of the stellar kinematics in the bulge indicates cylindrical rotation that can be explained without recourse to a non-axisymmetric distribution function (Shaw et al. 1993). However, Merrifield & Kuijken (1999) have recently argued for a bar based on the peculiar [N II] emission-line profiles along the major axis of NGC 3079. The situation for NGC 4388 is equally ambiguous. Recent K-band imaging by McLeod & Rieke (1995) revealed a boxy bulge, but the nearly edge-on aspect of this galaxy prevented them from detecting the morphological signature of a bar.

The two-dimensional velocity fields that we will present in this paper reveal unambiguously a bar potential in both NGC 3079 and NGC 4388. Contrary to previous work based on long-slit

spectra (e.g., Kuijken & Merrifield 1995; Merrifield & Kuijken 1999; Bureau & Freeman 1999), our detection of the bar potential in these two galaxies does not rely on an inner Lindblad resonance ( $x_2$ -like orbits) or strong bar-induced shocks that split emission-line profiles when the bar is seen edge-on.

Our paper is organized as follows. In §2, we briefly describe the methods used to obtain and reduce the near-infrared images and optical Fabry-Perot observations. Results on NGC 3079 and NGC 4388 are discussed in §3 and §4, respectively. For each galaxy, we first analyze the morphology of the stellar bulge and its degree of boxiness. Next, we use the observed velocity field of the ionized gas to argue for a bar potential. Self-consistent dynamical interpretation of the disk velocity field requires analysis of the surface photometry to constrain the mass distribution, a task beyond the scope of this paper. The models presented here are purely kinematical in nature, but they show the clear kinematic signature of bar streaming motions in both objects. In §5, we discuss the implications of our results using the predictions of bar evolutionary models, and attempt to quantify how bars fuel the nuclear activity. We summarize our results in §6 along with future avenues of research.

## 2. Observations and Data Reduction

### 2.1. Fabry-Perot Spectroscopy

During the course of our spectroscopic survey of active galaxies with extended line-emitting regions, we obtained a large Fabry-Perot datacube ( $x, y, \lambda$ ) of NGC 3079 that spans the  $H\alpha + [N II] \lambda\lambda 6548, 6583$  emission-line complex, and two datacubes of NGC 4388 centered on the  $H\alpha$  and  $[O III] \lambda 5007$  emission lines. Observational parameters of the Fabry-Perot spectra are listed in Table 1. The observational setup and reductions used to obtain and reduce these data have been detailed elsewhere (VCBTFS, VBCTM, and Veilleux, Cecil, & Bland-Hawthorn 1995; hereafter VCB). In both NGC 3079 and NGC 4388, the observed emission-line profiles were parameterized by simple Gaussian functions. Deviations from Gaussians will be discussed in §5.1. The best fits were determined by the least- $\chi^2$  method on spectrally smoothed emission line profiles using a  $1/4 - 1/2 - 1/4$  spectral filter (Hanning smoothing). Spatial Gaussian smoothing with  $\sigma = 1$  pixel was used to improve the sensitivity to fainter features. For the  $H\alpha + [N II] \lambda\lambda 6548, 6583$  complex in NGC 3079, an iterative fitting method was used whereby all parameters of the three Gaussian profiles were first left unconstrained (except for the  $[N II] \lambda 6583/\lambda 6548$  ratio which was fixed to its quantum value, 2.98; Osterbrock 1989). The continuum levels and centroids of the  $H\alpha$  and  $[N II]$  profiles determined from this first iteration were then used as input parameters for a second iteration.

## 2.2. Infrared Imaging

Infrared images of NGC 3079 and NGC 4388 were obtained in the course of imaging surveys of nearby galaxies by R. B. Tully and by S. Courteau and J. Holtzman, respectively. We thank our colleagues for providing us with their data. On June 23 1993, the University of Hawaii 2.2-meter telescope on Mauna Kea equipped with the NICMOS-3 camera (Hodapp, Rayner, & Irwin 1992) was used to obtain a  $K'$ -band image of NGC 3079. This imaging system uses a  $256 \times 256$  pixel NICMOS-3 HgCdTe detector array and interchangeable reimaging lenses to provide two spatial scales. The large angular size of the program galaxies required the 2:1 reducing optics, resulting in a field of  $\sim 3'$  square at a scale of  $0''.75 \text{ pixel}^{-1}$ . The  $K'$  filter described in Wainscoat & Cowie (1992) minimized the thermal background. The integration time for each frame was 1 minute, and the total exposure on NGC 3079 was 6 minutes.

The H-band image of NGC 4388 was obtained on April 28, 1994 using the Cryogenic Optical Bench (COB) on the KPNO 2.1-meter telescope. This system uses a  $256 \times 256$  pixel InSb detector array, and provides a field of  $\sim 2'$  square at a scale of  $0''.50 \text{ pixel}^{-1}$ . The total exposure on NGC 4388 was 1,000 seconds.

Both image sets were reduced using standard techniques (e.g., Hodapp et al. 1992; McCaughrean 1989), and were not flux calibrated because we are only interested in the bulge/disk structure.

## 3. Results on NGC 3079

### 3.1. Stellar Morphology

The  $K'$ -band image of NGC 3079 is shown in Figure 1a, rotated to place the photometric major axis of the galaxy vertically. This axis was found to be along  $\text{PA}_{\text{maj}} = 169^\circ \pm 4^\circ$ , in good agreement with the results of Irwin & Seaquist (1991;  $\text{PA}_{\text{maj}} = 166^\circ$ ). Also shown are two simple photometric models of the galaxy. In Figure 1c, the isophotes representing the sum of an exponential disk and a spherically symmetric bulge are shown, emphasizing the boxiness of the observed bulge. An attempt is made in Figure 1b to model the observed isophotes more accurately with a box-shaped structure of the form  $I = I_{\text{box}} + I_{\text{disk}}$  where

$$I_{\text{box}} = I_{b0} \left( 1 + \left| \frac{R}{a} \right|^p + \left| \frac{z}{b} \right|^p \right)^{-1/p}, \quad (1)$$

$$I_{\text{disk}} = I_{d0} \exp\left(-\frac{R}{R_s}\right) \exp\left(-\frac{|z|}{z_s}\right). \quad (2)$$

This analytic formulation of the boxy structure was first introduced by Pfenniger & Friedli (1991). The parameters of the best fit model are  $I_{b0}/I_{d0} = 4.6$ ,  $a : b = 1 : 0.43$ ,  $p = 3.5$ ,  $R_s = 3.0 \text{ kpc}$ , and  $z_s = 380 \text{ pc}$  (for an inclination of  $82^\circ$ , §3.2.2). For comparison, the spherically symmetric bulge in Figure 1c has  $I_{b0}/I_{d0} = 1.8$ ,  $b : a = 1 : 1$ , and  $p = 2$ .

The residual image after subtracting the boxy model from the data is shown in Figure 1*d*. The striking X-structure in the central region indicates a peanut-shaped bulge. Although the boxiness of the bulge in this galaxy has been known for some time (e.g., Shaw 1987; Young, Claussen, & Scoville 1988; Shaw et al. 1993), our infrared image emphasizes its importance by minimizing emission from the young stellar disk and the effects of dust. A detailed comparison of Figure 1*a* and Figure 3 from VCB indicates that the lower portions of the X-shaped line-emitting filaments reported by VCB do *not* coincide spatially with the peanut-shaped residual observed at infrared wavelengths. The boxiness of the infrared isophotes is therefore unlikely to be due to hot dust or line emission from the X-shaped filaments.

Also visible in the residual image is a well-defined warp to the north-west. A southern warp may also be present, but broader spatial coverage is needed to see if it bends east (“integral sign” warp) or west (warp with mirror symmetry with respect to the minor axis). The distributions of line-emitting (VCB) and H I gas (Irwin & Seaquist 1991) strongly favor the former orientation.

Finally, note the large residual nuclear core and disk in Figure 1*d*. This nuclear disk coincides roughly with the molecular disk and nuclear starburst in this galaxy (Lawrence et al. 1985; Young, Claussen, & Scoville 1988; Irwin & Sofue 1992; Sofue & Irwin 1992; Baan & Irwin 1995).

### 3.2. Kinematics of the Gaseous Galactic Disk

#### 3.2.1. General Description

Figure 2*a* reproduces the distribution of line-emitting gas derived from our Gaussian fits that was presented in VCB. The velocity fields from these data are shown in Figures 2*b* and 2*c*. The uncertainty on these velocities is  $\sim 35 \text{ km s}^{-1}$  in the brighter disk H II regions, but may be 2-3 times larger in the fainter material outside of the disk. The H $\alpha$  and [N II]  $\lambda 6583$  velocity fields shown in Figures 2*b* and 2*c* generally agree within these errors.

In these figures a string of black dots traces the steepest gradient through the observed velocity field (using the method described in Bland 1986); this is the kinematic line of nodes. Figure 3 shows the H $\alpha$  rotation curve lay along this locus. It rises linearly in the inner region and flattens to  $\sim 245 \pm 25 \text{ km s}^{-1}$  (or a deprojected value of  $\sim 250 \pm 25 \text{ km s}^{-1}$  if  $i = 82^\circ$ ; §3.2.2) beyond a radius of  $\sim 1 \text{ kpc}$ . A systemic velocity of  $\sim 1150 \pm 25 \text{ km s}^{-1}$  is derived from this rotation curve. This value agrees well with estimates from other optical datasets (e.g.,  $1177 \text{ km s}^{-1}$  from Humason et al. 1956;  $1150 \text{ km s}^{-1}$  from Carozzi 1977) and CO spectra (e.g.,  $1150 \text{ km s}^{-1}$  from Sofue & Irwin 1992), but slightly exceeds the value derived from HI data (e.g.,  $1120 \text{ km s}^{-1}$  from Rots 1980;  $1125 \text{ km s}^{-1}$  from Fisher & Tully 1981;  $1118 \pm 3 \text{ km s}^{-1}$  from Staveley-Smith & Davies 1988;  $1124 \pm 10 \text{ km s}^{-1}$  from Irwin & Seaquist 1991). This apparent discrepancy is probably due to a slight asymmetry between the inner optical/CO rotation curve ( $R \lesssim 8 \text{ kpc}$ ) and the outer H I rotation curve. First noted by Sofue (1996), this asymmetry may arise from

a misaligned dark halo or tidal interaction with nearby companions such as NGC 3073. The systemic velocity derived from optical spectra of the stellar bulge of NGC 3079 is closer to the HI value ( $1114 \pm 9 \text{ km s}^{-1}$  from Shaw et al. 1993).

Well-defined ‘tongues’ of highly redshifted (blueshifted) gas extend immediately south (north) of the nucleus. Interestingly, these two ‘tongues’ are slightly misaligned at the nucleus. The kinematic line of nodes also jumps  $10^\circ$  clockwise on either side of the nucleus immediately outside the ‘tongues’ ( $R \gtrsim 2.5 \text{ kpc}$ ; Fig. 2), then twists slightly anti-clockwise. This complex behavior may arise from a combination of (1) a warp in the galactic disk, (2) patchy dust obscuration, (3) streaming motion along spiral arms, and (4) eccentric orbits aligned with a bar. Although dust may contribute to the slight large-scale differences between the present optical data and the H I data of Irwin & Seaquist (1991), the near-perfect bisymmetry of the velocity field near the center of the galaxy strongly suggests that dust insignificantly affects the observed velocity field. Similarly, the photometric warp detected on the outskirts of the galaxy at optical, infrared, and radio wavelengths, does not affect the kinematics of the gas inside a radius of  $\sim 8 \text{ kpc}$ . Finally, the coincidence between the clockwise shift in the kinematic line of nodes and the anti-clockwise “spiral arms” seen on the K'-band image of NGC 3079 (Fig. 1a) in both the northern and southern sections of the disk is good evidence for elliptic streaming through the spiral arms. However, this type of streaming motion cannot explain the peculiarities of the velocity field near the central region.

‘Twisting’ of the isovelocity contours in the central portion of galaxies often signals a bar potential (e.g., Kalnajs 1978; Roberts, Huntley, & van Albada 1979; Sanders & Tubbs 1980; Schwarz 1981). The nuclear offset between the two ‘tongues’ in NGC 3079 can arise in this manner, as described next.

### 3.2.2. Kinematic Models

We began our analysis by exploring the parameter space for an axisymmetric disk with inclination  $50^\circ \leq i \leq 90^\circ$ , kinematic major axis  $160^\circ \leq \text{PA} \leq 200^\circ$ , and systemic velocity  $1,000 \leq V_{\text{sys}} \leq 1,300 \text{ km s}^{-1}$ . This region of parameter space was selected based on the results of previous optical and HI kinematic studies of NGC 3079 (see references in the previous section). A smoothed (flux-weighted) version of the rotation curve derived along the kinematic line of nodes (Fig. 3) was used for the analysis. When searching for the best-fitting model, the whole disk out to  $R \approx 12 \text{ kpc}$  was considered. Deviations from Gaussian profiles were not considered in the following analysis (see §5.1). Dust obscuration, one likely source of profile asymmetry in this highly inclined galaxy, is also not included in the models.

Figure 4 shows the best-fitting axisymmetric model ( $i = 82^\circ$ ,  $\text{PA} = 169^\circ$ , and  $V_{\text{sys}} = 1,150 \text{ km s}^{-1}$ ). Figure 4c shows the residuals after subtracting the model from our measured  $\text{H}\alpha$  velocity field. We conclude that an axisymmetric model does not fit the observed velocity field.

To look for the kinematic signature of a bar in NGC 3079, we constructed more elaborate models of gas motions in the inner disk that are similar to those described in Staveley-Smith et al. (1990). We model the intrinsic gas orbits as nonintersecting, inclined elliptical annuli that conserve angular momentum (so there are no hydrodynamic shocks or gas flows near the corotation radius or in the bar; Athanassoula 1992; Piner, Stone, & Teuben 1995). The ellipticity was held constant within a radius  $R_b$ , then was assumed to decrease linearly out to a radius  $R_d$  where the orbits are circular.

The velocity field for the best fitting model is shown in Figure 4*b*; model parameters are listed in Table 2. Our model invokes a bar with moderately eccentric orbits ( $e = b/a = 0.7$ ) with  $R_b = 3.6$  kpc and  $R_d = 6.0$  kpc aligned along  $PA = 130^\circ \pm 10^\circ$  intrinsic to the disk. This projects to  $PA = 97^\circ$  on the sky [using  $\tan(PA_{\text{obs}}) = \tan(PA_{\text{intrinsic}})\sec i$ ]. The position angle of the bar is well constrained by our models. When the bar is close to the major or minor axis, one does not get the twist of the line of node in the center, nor the NW-SE bisymmetric structure at large radius. In this respect, the intermediate angle bar models are a great success. Compared to the model with purely circular motions (Fig. 4*c*), the model that incorporates elliptical streaming has significantly smaller residuals in the central portion of the disk (Fig. 4*d*). The dispersion in the residuals within the inner disk ( $R \lesssim 6$  kpc) is only  $34 \text{ km s}^{-1}$  compared to  $40 \text{ km s}^{-1}$  for models without the bar.

## 4. Results on NGC 4388

### 4.1. Stellar Morphology

The top panel of Figure 5 shows the H-band image of NGC 4388. The position of the photometric major axis of NGC 4388 derived from this image is  $PA_{\text{maj}} = 90^\circ \pm 4^\circ$ . As for NGC 3079, we attempted to model the morphology of NGC 4388 using either the sum of an exponential disk and a spherically symmetric bulge (Fig. 5*c*) or the sum of an exponential disk and a box-shaped bulge (eqns 1 & 2; Fig. 5*b*). The second solution clearly fits the data better. The parameters of this model are  $I_{b0}/I_{d0} = 5.0$ ,  $a : b = 1:0.35$ ,  $p = 3.5$ ,  $R_s = 1.8$  kpc, and  $z_s = 0.32$  pc (for inclination  $-78^\circ$ , derived from our kinematic data; §4.2.2).

The residuals after subtracting this model from the data are shown in Figure 5*d*. Residual spiral arms run east-west in the galactic plane and coincide spatially with strings of HII regions in the  $H\alpha$  emission-line image (see Fig. 1*a* of VBCTM). The excess H-band emission at these star-forming complexes is probably due to young supergiant stars. A bright fan-like residual is also visible slightly south of the nucleus, coincident with bright  $H\alpha$  and [O III] emission. Some of this residual emission comes from the AGN in NGC 4388 (VBCTM).



## 4.2. Kinematics of the Gaseous Galactic Disk

### 4.2.1. General Description

The emission-line maps and velocity fields derived from the  $H\alpha$  and [O III]  $\lambda 5007$  data cubes were presented by VBCTM; the velocity fields are reproduced in Figure 6. Uncertainties range from  $\sim 20$  km s $^{-1}$  in the bright line-emitting regions to  $\gtrsim 100$  km s $^{-1}$  in the fainter areas. The ellipse superposed on this figure differentiates between material in the disk and beyond. A clear kinematic dichotomy is evident. The models described in the next section seek to reproduce the velocity field of the disk material. The kinematics of the extraplanar gas are discussed in detail in VBCTM.

The velocity field of the [O III]-emitting gas in the disk resembles that of the  $H\alpha$ -emitting gas. It is characterized by a large-scale east-west gradient that indicates rotation in the galactic disk. Figure 7 shows the rotation curve derived along the line of nodes of the  $H\alpha$  velocity field. The rotation curve derived from our data is consistent with earlier results (cf. Rubin, Kenney, & Young 1997 and references therein). The systemic velocity derived from this rotation curve ( $2,525 \pm 25$  km s $^{-1}$ ) also agrees with published values ( $2515 \pm 7$  km s $^{-1}$  from Helou et al. 1981;  $2,529 \pm 3$  km s $^{-1}$  from Corbin, Baldwin, & Wilson 1988;  $2,554 \pm 39$  km s $^{-1}$  from Ayani & Iye 1989;  $2,525 \pm 15$  km s $^{-1}$  from Petitjean & Durret 1993;  $2,538 \pm 26$  km s $^{-1}$  from de Vaucouleurs et al. 1991;  $2,502 \pm 10$  km s $^{-1}$  from Rubin, Kenney, & Young 1997). ‘Twisting’ of the isovelocity contours is clearly visible in the central  $1'$  diameter of NGC 4388. As for NGC 3079, the near-perfect bisymmetry of the velocity field in the central region of the galaxy strongly suggests that dust does not significantly affect the observed velocity field there. The kinematic models described in the next section indicate that the velocity field is best generated by a bar.

### 4.2.2. Kinematic Models

Our kinematic models seek to reproduce the  $H\alpha$  velocity field. In choosing the  $H\alpha$  data for this analysis we have tried to minimize effects associated with nuclear activity. Dynamical processes such as entrainment by AGN-powered radio jets generally have a stronger effect on the kinematics of the highly ionized [O III]-emitting gas than on those of the low-ionization  $H\alpha$ -emitting material (e.g., Whittle et al. 1988).

The procedure used to find the best-fitting model for NGC 4388 followed the same steps as for NGC 3079. First, we explored the parameter space for an axisymmetric disk with inclination  $-90^\circ \leq i \leq -50^\circ$ , kinematic major axis along  $70^\circ \leq \text{PA} \leq 110^\circ$ , and a systemic velocity of  $2,400 \leq V_{\text{sys}} \leq 2,600$  km s $^{-1}$  (this range in the parameters brackets the results of previous kinematic studies; see references in §4.2.1). Note that the negative inclination means that the north rim of the disk is the near side. This is consistent with the morphology of the high-ionization gas as explained in VBCTM. Under these conditions, the two spiral arms of bright HII regions are

trailing rotation, as generally arises in spiral galaxies. To simplify the analysis, we used a smooth (projected) rotation curve of the form:

$$V = V_0 \frac{[1 - \exp(-\alpha R)]}{[1 - \exp(-\alpha)]} + V_{\text{sys}}, \quad (3)$$

where  $R$  is the galactocentric radius in arcseconds. Deviations from Gaussians were not considered in our analysis (see §5.1).

Figure 8a shows the best-fitting axisymmetric model ( $i = -78^\circ$ ,  $\text{PA} = 90^\circ$ ,  $\alpha = 0.10 \text{ arcsec}^{-1}$ ,  $V_0 = 180 \text{ km s}^{-1}$  and  $V_{\text{sys}} = 2,525 \text{ km s}^{-1}$ ) and the result of subtracting it from the  $\text{H}\alpha$  velocity field. The residuals in Figure 8c are significant and reveal substantial non-circular motion. Variations in the rotation curve do not improve significantly the quality of the fit.

Plausible dynamical origins for the non-circular motions in the disk include forcing by a bar or oval distortion, density wave streaming associated with the spiral arms, and disk warping. Our spectra span only the inner 5 kpc of the disk, so the last effect is unimportant. A stellar bar has been suggested previously based on the morphology of the central region, but no consensus has emerged on its position angle (Phillips & Malin 1982:  $30^\circ$ ; Corbin, Baldwin, & Wilson 1988:  $30^\circ$ ; Colina et al. 1987:  $130^\circ$ ; see also Rubin et al. 1997). Figure 8b presents the best fitting model that incorporates elliptical streaming; Table 2 lists the model parameters. The fit used a smooth rotation curve of form (3) ( $V_0 = 180 \text{ km s}^{-1}$ ,  $\alpha = 0.10 \text{ arcsec}^{-1}$ ). Our model involves a bar with radius  $R_b = 1.5 \text{ kpc}$  and highly eccentric orbits ( $e = 0.3$ ) aligned along  $\text{PA} = 135^\circ$  intrinsic to the disk. This projects to  $\text{PA} = 100^\circ$  on the sky. The spiral-arm effect arises because the gas orbits become increasingly less elliptical from the ends of the bar to the edge of the disk ( $e = 1$  at the edge of the disk,  $R_d \approx 5 \text{ kpc}$ ), and the intrinsic bar PA going from  $135^\circ$  to  $90^\circ$ . Elliptical streaming significantly reduces the velocity residuals (Fig. 8d). The residuals present a highly symmetric Gaussian distribution with a dispersion of only  $20 \text{ km s}^{-1}$ . The fit is remarkably good considering that hydrodynamic effects (e.g., strong shocks along the bar; Athanassoula 1992; Piner, Stone, & Teuben 1995) and dust obscuration are not modeled.

## 5. Discussion

### 5.1. Additional Kinematic Evidence for Stellar Bars in NGC 3079 and NGC 4388?

Strong kinematic evidence for bar streaming motions in NGC 3079 and NGC 4388 was presented in §3.2 and §4.2, respectively. The velocity fields used for this analysis were derived by fitting Gaussians to the emission-line profiles. Deviations from Gaussians were detected in the inner disk of both galaxies. In NGC 3079, emission-line profiles are split north of the nucleus ( $\text{PA} \approx -10^\circ$ , i.e. along the disk) out to a radius of  $\sim 16''$  (1.3 kpc), but in a sector only  $\sim 2 - 3''$  (170 – 335 pc) wide. The degree of line splitting varies smoothly with radius, first increasing monotonically to  $\sim 275 \text{ km s}^{-1}$  at 200 – 300 pc radii, beyond which it decreases. These anomalous

line profiles were described in Filippenko & Sargent (1992; their Fig. 2) and VCBTFS (their Fig. 11a). Split line profiles were also detected by Irwin & Sofue (1992) in the inner  $\text{H}_2$  molecular disk of this galaxy. Similar line splitting with maximum amplitude  $\sim 150 \text{ km s}^{-1}$  is observed on both sides of the nucleus of NGC 4388 out to radii of  $\sim 10''$  along the disk ( $\sim 1 \text{ kpc}$ ; see also Iye & Ulrich 1986; Colina et al. 1987; Ayani & Iye 1989; Veilleux 1991; Rubin et al. 1997).

The origin of this line splitting is unclear. VCBTFS tentatively interpreted the line splitting in the inner disk of NGC 3079 as being due to the effects of the nuclear outflow on the gaseous component of the galactic disk (see also Sofue & Irwin 1992). Rubin et al. (1997) have argued that the anomalous kinematics in the inner disk of NGC 4388 indicates the presence of a discrete rapidly rotating circumnuclear disk. We argue that bar-induced noncircular motions may also split the lines. Kuijken & Merrifield (1995) and, more recently, Bureau & Athanassoula (1999) have pointed out that the line-of-sight velocity distribution of both the gaseous and stellar components in barred potentials observed edge-on may be double-peaked and characterized by a “figure-of-eight” variation with radius out to roughly the end of the bar. Their conclusions have since been confirmed by hydrodynamical gas simulations (Athanassoula & Bureau 1999). Some of these simulations reproduce remarkably well the velocity field of the inner disk of NGC 4388 (e.g., Fig. 3 of Rubin et al. 1997). The line splitting in this galaxy is symmetric with respect to the nucleus and extends out to near the end of the stellar bar. The small extent of the line splitting in NGC 3079 relative to the size of the bar ( $R_b = 3.6 \text{ kpc}$ ) and its asymmetry with respect to the nucleus are more difficult to explain in this scenario, but selective dust obscuration by material in the disk may account for some of the asymmetry (see also long-slit observations of this galaxy by Merrifield & Kuijken 1999).

## 5.2. The Bar – Boxy Bulge Connection

The co-existence of stellar bars and boxy bulges in NGC 3079 and NGC 4388 brings additional observational support to evolutionary models which posit that box/peanut-shaped bulges of disk galaxies arise from a vertical instability in bars. Given bars in both galaxies, there is no need to invoke accretion to explain the boxy bulges in these galaxies (e.g., May, van Albada, & Norman 1985; Binney & Petrou 1985; Rowley 1986, 1988). Note, however, that we cannot exclude the possibility that each bar was created by a galaxy interaction or merger and then evolved into a boxy bulge through the bar-buckling instability (e.g., Noguchi 1987; Gerin, Combes, & Athanassoula 1990; Hernquist, Heyl, & Spergel 1993; Mihos et al. 1995; Miwa & Noguchi 1998).

Evolutionary models which invoke resonant heating of the bar (Combes et al. 1990; Pfenniger & Norman 1990; Pfenniger & Friedli 1991) predict the formation of a boxy bulge over  $\sim 10$  bar rotations. The bulge may form even quicker if the bar is subject to bending or fire-hose instabilities (Raha et al. 1991; Merritt & Sellwood 1994). The bar rotation periods in NGC 3079 and NGC 4388 can be derived assuming that the bars end near the corotation radius and using the observed rotation velocities there. We find  $\tau_{\text{bar}}(\text{NGC 3079}) \approx \tau_{\text{bar}}(\text{NGC 4388}) \simeq 1 \times 10^8 \text{ yrs.}$

The boxy bulges in both NGC 3079 and NGC 4388 were therefore formed over  $\lesssim 10^9$  yrs.

The rate of bar heating/bulge formation is also a strong function of the central mass concentration in these galaxies (e.g., Norman, May, & van Albada 1985; Hasan & Norman 1990; Friedli & Pfenniger 1991; Friedli & Benz 1993, 1995; Hasan, Pfenniger, & Norman 1993; Norman, Sellwood, & Hasan 1996; Merritt & Quinlan 1998; Sellwood & Moore 1999). Large mass concentrations create inner-Lindblad resonances (ILRs). ILRs form the anti-bar orbit families  $x_2$  and  $x_3$ , which thereby weaken the stellar bar.

Simulations (Norman et al. 1996; and Merritt & Quinlan 1998) suggest that the bar may be destroyed within a fraction of its rotation period if the core mass exceeds  $\sim 1 - 5\%$  of the combined disk and bulge mass. Is this condition met in NGC 3079 and NGC 4388? An estimate of the core mass can be derived assuming the nuclear activity is due to accretion around a black hole of mass comparable to that of the galaxy core. Recent compilations of black hole masses (Kormendy et al. 1997; Richstone 1998; Magorrian et al. 1998) suggest a rough proportionality between black hole and bulge masses with  $M_{\text{BH}} \simeq 0.005 M_{\text{bulge}}$ . The constant of proportionality may depend slightly on morphological type, perhaps increasing from late- to early-type galaxies (e.g.,  $M_{\text{BH}} \sim 2.5\% M_{\text{bulge}}$  in the S0 galaxies NGC 3115 and NGC 4342; Merritt 1998), but this variation is of little importance here because we are dealing with two late-type galaxies. In this case, we get

$$\eta \equiv \frac{M_{\text{core}}}{M_{\text{bulge}} + M_{\text{disk}}} \simeq \frac{M_{\text{BH}}}{M_{\text{bulge}} + M_{\text{disk}}} \simeq 0.005 \frac{M_{\text{bulge}}}{M_{\text{bulge}} + M_{\text{disk}}} \lesssim 0.005, \quad (4)$$

implying that the central black holes in these galaxies do not play a significant role in the destruction of the bars. The very presence of AGN in NGC 3079 and NGC 4388 may *require*  $\eta$  to be smaller than the critical value for rapid bar dissolution because destruction of the bar would end mass accretion onto the nucleus (see Merritt 1998).

The short time scales that we derive suggest that we are unlikely to have caught the bars in the act of forming boxy bulges. This is probably also the case for most barred spirals with boxy bulges, given the large fraction of disk galaxies with strong bars ( $\sim 35\%$ ; e.g., Shaw 1987; Sellwood & Wilkinson 1993; Mulchaey & Regan 1997) and box-peanut bulges (20 – 45%; e.g., Jarvis 1986; Shaw 1987; de Souza & dos Anjos 1987; Dettmar & Barteldrees 1988, 1990; see Dwek et al. 1995, Kuijken 1996, and references therein for a discussion of our own Galaxy). Numerical simulations suggest that bars can indeed persist after the epoch of boxy bulge formation (e.g., Miller & Smith 1979; Pfenniger & Friedli 1991; but see Raha et al. 1990 for a counterexample). It is also possible that bar formation, dissolution, and bulge building recurs in disk galaxies. Open-box simulations of disk galaxies with nearby companions show that tidal encounters can repeatedly form a bar throughout the life of a disk galaxy (e.g., Sellwood & Moore 1999).

### 5.3. Stellar Bars and Nuclear Activity

Stellar bars in NGC 3079 and NGC 4388 do not necessarily assure efficient fueling of the nuclear starbursts/AGN. Our kinematic models neglect hydrodynamical effects and therefore cannot constrain the bar-induced mass inflow rates in these galaxies. Several factors are important in determining if these bar-induced mass inflow rates suffice to power the observed nuclear activity. Possibly relevant parameters include the strength and length of the bar, the gas mass-fraction and morphological type of the host galaxy, the star formation efficiency, the age of the bar, and the existence of ILRs near the nucleus. In this section, we review briefly each of these possibilities in the context of NGC 3079 and NGC 4388.

#### 5.3.1. Length and Strength of the Bar

Surveys of barred galaxies find that those currently displaying the highest star formation activity have both strong and long bars (e.g., Martin 1995; Martinet & Friedli 1997). Here, we follow Martinet & Friedli and define strong and long bars as having deprojected bar axis ratios  $(b/a)_i \leq 0.6$  and relative lengths  $2L_i/D_{25} \geq 0.18$  where  $L_i$  is the deprojected bar length and  $D_{25}$  is the galaxy diameter at 25 mag arcsec<sup>-2</sup>. The high inclinations of NGC 3079 and NGC 4388 prevent us from determining photometrically the lengths and axis ratios of these bars, but the results from our analysis of the velocity fields (Table 2) constrain these values. Assuming  $L_i \approx R_b$  and using  $D_{25} = 40$  kpc for NGC 3079 and 27 kpc for NGC 4388 (de Vaucouleurs et al. 1991), we get relative lengths of  $\sim 0.18$  and  $\sim 0.11$  for NGC 3079 and NGC 4388, respectively. The bar in NGC 3079 therefore is a borderline case while that of NGC 4388 appears to be a short bar. The strengths of the bars may be estimated using the derived eccentricity ( $= b/a$ ) of the gas orbits in the inner ( $R \leq R_b$ ) portion of the bars. The bar in NGC 4388 would therefore be considered a strong bar while that in NGC 3079 is weak. Note, however, that using the eccentricity of the gas orbits rather than that of the stellar orbits probably overestimates the strength of the stellar bar by factors of 2 – 3 (e.g., Friedli & Benz 1993), so that even the bar in NGC 4388 may be relatively weak. The modest size and weakness of the stellar bars in both galaxies may prevent efficient fueling of their active nuclei.

#### 5.3.2. Gas Mass Fraction, Morphological Type, and Star Formation Efficiency

That not all galaxies with strong and long bars are forming stars furiously (Martinet & Friedli 1997) indicates that other parameters also affect the star formation rate in barred galaxies. The numerical simulations of Friedli & Benz (1995) suggest that the overall rate of star formation increases with gas mass-fraction of the galaxy. These authors found that a larger gas mass-fraction pushes the threshold for star formation to larger radii in the disk, thereby increasing the overall star formation rate. However, feedback between star formation and the release of mechanical

energy from supernovae keeps the rate of star formation in the central regions relatively constant. This may explain why the correlation between gas mass-fraction and *nuclear* star-formation is more evident in early-type barred spirals, where star formation rates and feedback from supernovae are more modest (e.g., Hawarden et al. 1986; Devereux 1987; Dressel 1988; Arsenault 1989; Huang et al. 1996).

For NGC 3079, little can therefore be said on the importance of the gas mass-fraction in determining bar-induced fueling. However, it is clear that the nuclear starburst in this galaxy has the potential to be long-lived regardless of the mass inflow rate induced by the bar. Indeed, given the current star formation rate in the nucleus ( $\sim 10 \beta^{-1} M_{\odot} \text{ yr}^{-1}$  where  $\beta < 1$  is the fraction of the bolometric luminosity of NGC 3079 radiated by stars; VCBTFS) and the total mass of atomic and molecular gas observed in the galaxy *core* (Irwin & Seaquist 1991), star formation will deplete gas in the nuclear region of NGC 3079 in  $> \beta 10^9$  yrs. Bar-induced inflow would increase this time.

The situation in NGC 4388 is less clear because the nuclear activity appears to be powered by an AGN rather than a starburst. We are unaware of numerical simulations that address the effects of gas mass-fraction or morphological type on the level of AGN activity.

### 5.3.3. Age of the Bar

Self-consistent evolutionary models of barred galaxies by Friedli & Benz (1995), Martinet & Friedli (1997) and Martin & Friedli (1997) suggest that both the total and nuclear star formation rates in galaxies with strong (weak) bars peak  $\lesssim 1$  (2) Gyr after the bar instability starts. The *relative* importance of nuclear star formation increases more than tenfold over that time span. According to strong (weak) bar simulations, young barred galaxies [ $\lesssim 0.5$  (1.0) Gyrs; Type A in the nomenclature of Martin & Friedli 1997] are characterized by chains of bright HII regions near strong shocks along the bar with no star formation activity in the nucleus, while old barred galaxies [ $\gtrsim 0.8$  (1.6) Gyrs; Type C] shows the opposite distribution. The discussion in §5.3.1 suggests that the time scales for the weak bar simulations are more likely to apply to the bars in NGC 3079 and NGC 4388. In principle, the star formation distribution in these bars can therefore constrain the age of the bars and determine if the bar is old enough to fuel the observed nuclear activity. Unfortunately, both NGC 3079 and NGC 4388 are highly inclined spirals and patchy dust obscuration affects the brightness of HII regions in these galaxies. Qualitatively, we find that the bar region in NGC 3079 presents a larger number of bright HII regions than that of NGC 4388, therefore suggesting that the stellar bar in NGC 3079 is less evolved than the one in NGC 4388.

Perhaps it is more instructive to invert this argument and attempt to constrain the age of the bar by assuming that the nuclear activity in NGC 3079 and NGC 4388 is induced by the bar. Then, the age of the bar should equal the sum of the starburst or AGN lifetime and the delay between bar formation and the onset of nuclear activity. This situation may be particularly

relevant to NGC 3079, where a nuclear starburst seems to power the kpc-scale windblown superbubble (VCBTFS). The dynamical time scale of the superbubble ( $\sim 10^6$  yrs; VCBTFS) and starburst age ( $10^7 - 10^8$  yrs) determined from the optical spectrum of the nucleus (VCBTFS) are both considerably shorter than the predicted delay between bar formation and the onset of the starburst ( $\sim 10^9$  yrs). If the starburst in NGC 3079 was triggered by the bar, this would imply that the bar is  $\sim 10^9$  yrs old. The age of the bar equals or exceeds the timescale that we derived in §5.2 for the formation of the boxy bulge in NGC 3079.

The situation is more complex in NGC 4388, where the nuclear activity is almost certainly due to mass accretion onto a supermassive black hole rather than from a starburst. The ionized gas detected above the disk of NGC 4388 (VBCTM) may be used to constrain the age of the AGN in this galaxy. This extraplanar material appears to be outflowing from the nucleus with a characteristic dynamical time scale of  $\sim 2 \times 10^7$  yrs. If no other outflows have occurred in NGC 4388, the dynamical time scale of the extraplanar material constrains the age of the AGN to a few  $\times 10^7$  yrs. Once again, this is much shorter than the predicted delay between the epoch of bar formation and the onset of starburst activity predicted by numerical simulations. However, more relevant to NGC 4388 is the delay between the epoch of bar formation and the onset of AGN activity. This delay depends critically on poorly constrained factors including star formation efficiency, the conversion efficiency of the kinetic energy injected from supernovae and stellar winds into gas motion (if both these efficiencies are large, less material will be available to fuel the AGN), and the time needed to transport material from the kpc-scale starburst down to the sub-pc scale of the AGN accretion disk. Simulations of AGN fueling by bars (e.g., Heller & Shlosman 1994) suggest that intense starburst activity always precedes or coincides with AGN activity. Our data can therefore only place a lower limit of  $\sim 10^9$  yrs on the age of the bar in NGC 4388. This is again consistent with the time scale that we derived for the formation of its boxy bulge.

#### 5.3.4. *Inner Lindblad Resonances*

In the self-consistent evolutionary models discussed in the previous section, the ILRs appear at the end of the simulations once sufficient mass has inflowed. ILRs have important consequences on the fueling of the nuclear starburst and perhaps the AGN. ILRs correspond to regions of orbit crowding associated with higher gas concentrations and sometimes accompanied by shocks (e.g., Athanassoula 1992; Piner et al. 1995). ILRs in barred galaxies often form a gas ring nearby (e.g., Telesco, Dressel, & Wolstencroft 1993). Gas flows down the dust lane of the bar to the ILR, then most sprays back into the bar region at the point of contact of the nuclear ring and the dust lane (e.g., Binney et al. 1991; Piner et al. 1995; Regan et al. 1997).

A galaxy can have zero, one, or two ILRs depending on its rotation curve and therefore on the detailed mass distribution. For a weak bar rotating with angular velocity  $\Omega_b$  in a galaxy in which stars at a galactocentric radius  $R$  (cylindrical coordinates) orbit with angular velocity  $\Omega(R) = V(R)/R$ , an ILR at that radius for which the bar potential perturbs, or drives, the stars

at a frequency equal to their natural (or epicyclic) frequency  $\kappa(R)$ ; i.e.  $\Omega_b = \Omega(R) - \kappa(R)/2$  at ILR where (e.g., Binney & Tremaine 1987):

$$\kappa(R)^2 = \frac{2V}{R} \left( \frac{V}{R} + \frac{dV}{dR} \right). \quad (5)$$

Our discussion in §5.3.1 suggests that this weak bar approximation is realistic for both galaxies. Unfortunately, we have no easy way to estimate  $\Omega_b$  in NGC 3079 and NGC 4388. We assume that the corotation radius,  $R_{\text{CR}}$  where  $\Omega_b = \Omega(R_{\text{CR}})$ , coincides with the ends of the bar (i.e.,  $R_{\text{CR}} \simeq R_b$ ), and derive  $\Omega_b \simeq 60 \text{ km s}^{-1} \text{ kpc}^{-1}$  in NGC 3079 and  $\Omega_b \simeq 105 \text{ km s}^{-1} \text{ kpc}^{-1}$  in NGC 4388. Next, we smoothed the rotation curves to calculate  $\kappa(R)$  from equation (5). For NGC 3079, we follow the procedure of Bland-Hawthorn, Freeman, & Quinn (1997) and fit the observed rotation using a dynamical model which comprises a Freeman exponential disk and a dark halo of the form

$$\rho_h = \rho_o (1 + r^2/r_a^2)^{-1} \quad (6)$$

with the rotation curve  $V(r)$  given by

$$V^2 = V_\infty^2 \left[ 1 - \left( \frac{r_a}{r} \right) \tan^{-1} \left( \frac{r}{r_a} \right) \right]. \quad (7)$$

This fitting procedure was not used for NGC 4388 because the nuclear outflow affects the velocity field north-east of the nucleus. Instead we deprojected equation (3) using  $V_0 = 180 \text{ km s}^{-1}$  and  $\alpha = 0.1 \text{ arcsec}^{-1}$ .

The results of our calculations are shown in the lower panels of Figures 9 and 10. The adopted rotation curves are shown in the top panels of these figures. We find that neither galaxy has an ILR. This result is consistent with the presence of large amounts of gas in the cores ( $\lesssim 1''$ ) of these objects. The absence of an ILR may help the bar-induced mass inflows continue down to nuclear scales to fuel the AGN and/or nuclear starburst. Note, however, that the converse may be generally false: results from numerical simulations suggest that ILRs do not necessarily prevent transport of material toward the nucleus (e.g., Friedli & Benz 1993). Consequently, the absence of an ILR in galactic nuclei is probably not a necessary condition for efficient fueling of AGN and nuclear starbursts.

## 6. Summary

In this paper, we have presented the first direct kinematic evidence for bar potentials in two active galaxies with box/peanut-shaped bulges. The complete two-dimensional coverage of our Fabry-Perot spectra has allowed us to detect the kinematic signature of the bar potential without an ILR or strong bar shocks. Our results provide observational support for bar evolutionary models where boxy bulges represent a critical transitional phase in the evolution of stellar bars into spheroidal bulges. We compared the predictions of these models with our data to determine that the boxy bulges in NGC 3079 and NGC 4388 probably formed over a time scale  $\lesssim 10^9$  yrs. This



short time scale, if typical of all barred galaxies, is difficult to reconcile with the high frequency of bars and boxy bulges in galaxies unless (1) bars survive the epoch of boxy bulge formation, or (2) bar and boxy bulge formation recur in the life of disk galaxies. Perhaps minor mergers reform a bar and feed new fuel to the host galaxy.

Stellar bars in NGC 3079 and NGC 4388 provide a mechanism for fueling the nuclear activity in these galaxies. However, we find no *direct* evidence that mass inflows induced by the bars suffice to power the nuclear activity in these objects. The bars in NGC 3079 and NGC 4388 are rather short and weak and may not be dynamically important enough to trigger the required mass inflows. Using the velocity fields and bar kinematics derived from the Fabry-Perot data, we find that both galaxies lack inner Lindblad resonances. This may explain the large quantities of gas found in the nuclei of these galaxies, and the fueling of these active galaxies down to a scale of 10 pc. However, our evaluation of the bar-induced fueling of the nuclear activity in these galaxies is severely limited by the current lack of simulations that attempt to relate the mass inflow rates outside  $\sim 10$  pc with the processes affecting gas dynamics closer in. Such simulations would be particularly relevant to NGC 4388 where the nuclear activity is probably due to an AGN (evidence for both a nuclear starburst and an AGN exists in NGC 3079). A proper treatment of the MHD effects associated with the AGN will be needed to address this important issue.

From an observational standpoint, more efforts should be made to search for small ( $\lesssim 10$  pc) nested bars in nearby active galaxies and to map the velocity field of the gaseous and stellar components in this region to constrain the dynamical importance of bars in fueling nuclear activity. As recent examples of such work, we note the intriguing results on Seyfert galaxies obtained by Regan & Mulchaey (1999) and Martini & Pogge (1999). Using the WFPC2 and NICMOS instruments on HST, they found a paucity of nuclear bars in the galaxies studied but several “nuclear mini-spirals”. Follow-up kinematical data may establish if such structures can fuel the AGN.

We thank S. Courteau, J. Holtzman, J. Huang, and R. B. Tully for acquiring and reducing the near-infrared images of NGC 3079 and NGC 4388 used in the present paper. We also thank the referee, R. Pogge, for constructive comments that helped improve the paper. SV is grateful for partial support of this research by a Cottrell Scholarship awarded by the Research Corporation, NASA/LTSA grant NAG 56547, NSF/CAREER grant AST-9874973, and Hubble fellowship HF-1039.01-92A awarded by the Space Telescope Science Institute which is operated by the AURA, Inc. for NASA under contract No. NAS5-26555. JBH acknowledges partial support from the Fullam award of the Dudley Observatory.

## REFERENCES

- Arsenault, R. 1989, *A&A*, 217, 66
- Athanassoula, E. 1992, *MNRAS*, 259, 345
- Athanassoula, E., & Bureau, M. 1999, *AJ*, in press (astro-ph/9904206)
- Ayani, K., & Iye, M. 1989, *AJ*, 97, 687
- Baan, W. A., & Irwin, J. A. 1995, *ApJ*, 446, 602
- Bahcall, J. N., Kirhakos, S., Saxe, D. H., & Schneider, D. P. 1997, *ApJ*, 479, 642
- Benedict, G. F., Smith, B. J., & Kenney, J. D. P. 1996, *AJ*, 111, 1861
- Bettoni, D., & Galletta, G. 1994, *A&A*, 281, 1
- Binney, J., Gerhard, O. E., Stark, A. A., Bally, J., & Uchida, K. I. 1991, *MNRAS*, 252, 210
- Binney, J., & Petrou, M. 1985, *MNRAS*, 214, 449
- Binney, J., & Tremaine, S. 1987, *Galactic Dynamics* (Princeton, Princeton Univ. Press)
- Bland, J. 1986, Ph.D. thesis, University of Sussex
- Bland-Hawthorn, J., Freeman, K. C., & Quinn, P. J. 1997, *ApJ*, 490, 143
- Bureau, M., & Athanassoula, E. 1999, *ApJ*, in press (astro-ph/9903061)
- Bureau, M., & Freeman, K. 1999, *AJ*, in press (astro-ph/9904015)
- Carozzi, N. 1977, *A&A*, 55, 261
- Colina, L., Fricke, K. J., Kollatschny, W., & Perryman, M. A. C. 1987, *A&A*, 186, 39
- Combes, F., & Sanders, R. H. 1981, *A&A*, 96, 164
- Combes, F., Debbasch, F., Friedli, D., & Pfenniger, D. 1990, *A&A*, 233, 82.
- Corbin, M. R., Baldwin, J. A., & Wilson, A. S. 1988, *ApJ*, 334, 584
- Courteau, S., De Jong, R. S., Broeils, A. H. 1996, *ApJ*, 457, L73
- Dahari, O. 1984, *AJ*, 89, 966
- de Robertis, M. M., Yee, H. K., & Hayhoe, K. 1998, *ApJ*, 496, 93
- de Souza, R. E., & dos Anjos, S. 1987, *A&A Suppl.*, 70, 465
- Dettmar, R.-J., & Barteldrees, A. 1988, *BAAS*, 20, 1085
- Dettmar, R.-J., & Barteldrees, A. 1990, *ESO/CTIO Workshop on Bulges of Galaxies, La Serena, Chile, Proceedings (A92-18101 05-90)*. Garching, ESO, p. 259-263.
- de Vaucouleurs, G., de Vaucouleurs, A., H. G. Jr. Corwin, Buta, R. J., Paturel, G., & Fouqué, P. 1991, *Third Reference Catalogue of Bright Galaxies* (New York, Springer-Verlag)
- Devereux, N. 1987, *ApJ*, 323, 91
- Dressel, L. L. 1988, *ApJ*, 329, L69

- Dultzin-Hacyan 1998, in IAU Symp. #186 Galaxy Interactions at Low and High Redshift, in press
- Dwek, E., et al. 1995, ApJ, 445, 716 Erwin, P. & Sparke, L. S. 1998, in Galaxy Dynamics, Proceedings of a Conference Held at Rutgers University, 9 - 12 August 1998, ed. D. R. Merritt, M. Valluri, and J. A. Sellwood, ASP Conf. Ser.
- Falcke, H., Wilson, A. S., & Simpson, C. 1998, ApJ, 502, 199
- Filippenko, A. V., & Sargent, W. L. W. 1992, AJ, 103, 28
- Fisher, J. R., & Tully, R. B. 1981, ApJS, 47, 139
- Ford, H. C., et al. 1994, ApJ, 435, L27
- Friedli, D., & Benz, W. 1993, A&A, 268, 65
- Friedli, D., & Benz, W. 1995, A&A, 301, 649
- Friedli, D., & Martinet, L. 1993, A&A, 277, 27
- Friedli, D., Wozniak, H., Rieke, M., Martinet, L., & Bratschi, P. 1996, A&AS, 118, 461
- Fuentes-Williams, T., & Stocke, J. T. 1988, AJ, 96, 1235
- Gerin, M., Combes, F., Athanassoula, E. 1990, A&A, 230, 37
- Hanson, C. G., Skinner, G. K., Eyles, C. J., & Wilmore, A. P. 1990,
- Hasan, H., & Norman, C. A. 1990, ApJ, 361, 69
- Hasan, H., Pfenniger, D., & Norman, C. 1993, ApJ, 409, 91
- Haschick, A. D., Baan, W. A., Schneps, M. H., Reid, M. J., Moran, J. M., & Gusten, R. 1990, ApJ, 356, 149
- Hawarden, T. G., Mountain, C. M., Leggett, S. K., & Puxley, P. J. 1986, MNRAS, 221, 41p
- Helou, G., Giovanardi, G., Salpeter, E. E., & Krumm, W. 1981, ApJS, 46, 267
- Heller, C. H., & Shlosman, I. 1994, ApJ, 424, 84
- Heraudeau, P., Simien, F., & Mamon, G. A. 1996, A&AS, 117, 417
- Hernquist, L., Heyl, J. S., & Spergel, D. N. 1993, ApJ, 416, L9
- Ho, L. C. 1996, PASP, 108, 637
- Ho, L. C., Filippenko, A. V., & Sargent, W. L. W. 1997, ApJ, 487, 591
- Hodapp, K.-W., Rayner, J., & Irwin, E. 1992, PASP, 104, 441
- Hohl, F., & Zang, T. A. 1979, AJ, 84, 585
- Huang, J. H., Gu, Q. S., Su, H. J., Hawarden, T. G., Liao, X. H., & Wu, G. X. 1996, A&A, 313, 13
- Humason, M. L., Mayall, N. U., & Sandage, A. R. 1956, AJ, 61, 97
- Hummel, E., & Saikia, D. J. 1991, A&A, 249, 43
- Irwin, J. A., & Seaquist, E. R. 1988, ApJ, 335, 658

- Irwin, J. A., & Seaquist, E. R. 1991, *ApJ*, 371, 111
- Irwin, J. A., & Sofue, Y. 1992, *ApJ*, 396, L75
- Isobe, T., & Feigelson, E. D. 1992, *ApJS*, 79, 197
- Iwasawa, K., et al. 1997, *MNRAS*, 285, 683
- Iye, M., & Ulrich, M.-H. 1986, *Astrophysics and Space Science*, 118, 523
- Jarvis, B. J. 1986, *AJ*, 91, 65
- Kalnajs, A. J. 1978, in *Structure and Properties of Nearby Galaxies*, eds. E. M. Berkhuisen and R. Wielebinski, 113
- Keel, W. C., & van Soest, E. T. M. 1992, *A&AS*, 94, 553
- Kennicutt, R. C., & Keel, W. C. 1987, *AJ*, 93, 1011
- Kormendy, J., et al. 1997, *ApJ*, 482, L139
- Kuijken, K., 1996, in *Barred Galaxies*, eds. R. Buta, D. A. Crocker, and B. G. Elmegreen (ASP: San Francisco), 505
- Kuijken, K., & Merrifield, M. R. 1995, *ApJ*, 443, L13
- Kukula, M. J., Pedlar, A., Baum, S. A., & O’Dea, C. P. 1995, *MNRAS*, 276, 1262
- Lawrence, A., Ward, M., Elvis, M., Fabbiano, G., Willner, S. P., Carleton, N. P., & Longmore, A. 1985, *ApJ*, 291, 117
- Maciejewski, W., & Sparke, L. S. 1997, *ApJ*, 484, L117
- Magorrian, J., et al. 1998, *AJ*, 115, 2285
- Martin, P. 1995, *AJ*, 109, 2428
- Martin, P., & Friedli, D. 1997, *A&A*, 326, 449
- Martini, P., & Pogge, R. W. 1999, *AJ*, submitted
- Martinet, L., & Friedli, D. 1997, *A&A*, 323, 363
- May, A., van Albada, T. S., & Norman, C. A. 1985, *MNRAS*, 214, 131
- McCaughrean, M. 1989, *Proceedings of the Third Infrared Detector Technology Workshop*, ed. C. R. McCreight (NASA Technical Memorandum, No 102209), 201
- McLeod, K. K., & Rieke, G. H. 1995, *ApJ*, 441, 96
- Merrifield, M. R., & Kuijken, K., & 1999, *A&A*, 345, L47
- Merritt, D. 1998, *Comments on Astrophysics*, 19, 000
- Merritt, D., & Quinlan, G. D. 1998, *ApJ*, 498, 625
- Merritt, D., & Sellwood, J. A. 1994, *ApJ*, 425, 551
- Mihos, J. C., Walker, I. R., Hernquist, L., Mendes de Oliveira, C., & Bolte, M. 1995, *ApJ*, 447, L87

- Miller, R. H., & Smith, B. F. 1979, *ApJ*, 227, 785
- Miwa, T., & Noguchi, M. 1998, *ApJ*, 499, 149
- Moles, M., Márquez, I., & Pérez, E. 1995, *ApJ*, 438, 604
- Mulchaey, J. S., & Regan, M. W. 1997, *ApJ*, 482, L135
- Noguchi, M. 1987, *MNRAS*, 228, 635
- Norman, C. A., May, A., & van Albada, T. A. 1985, *ApJ*, 296, 20
- Norman, C. A., Sellwood, J. A., & Hasan, H. 1996, *ApJ*, 462, 114
- Norman, C. A., & Silk, J. 1983, *ApJ*, 266, 502
- Osterbrock, D. E. 1989, *Astrophysics of Gaseous Nebulae and Active Galactic Nuclei*, (Mill Valley, University Science Books)
- Petitjean, P., & Durret, F. 1993, *A&A*, 277, 365
- Pfenniger, D., & Friedli, D. 1991, *A&A*, 252, 75
- Pfenniger, D., & Norman, C. 1990, *ApJ*, 363, 391
- Phillips, M. M., & Malin, D. F. 1982, *MNRAS*, 199, 205
- Piner, B. G., Stone, J. M., & Teuben, P. J. 1995, *ApJ*, 449, 508
- Pogge, R. W. 1988, *ApJ*, 332, 702
- Pompea, S. M., & Rieke, G. H. 1990, *ApJ*, 356, 416
- Quillen, A. C., Kuchinski, L. E., Frogel, J. A., & DePoy, D. L. 1997, *ApJ*, 481, 179
- Quillen, A. C., Frogel, J. A., Kenney, J. D., Pogge, R. W., & DePoy, D. L. 1995, *ApJ*, 441, 549
- Raha, N., Sellwood, J. A., James, R. A., & Kahn, F. D. 1991, *Nature*, 352, 411
- Regan, M. W., & Mulchaey, J. S. 1999, *ApJ*, 117, 2676
- Regan, M. W., Vogel, S. N., & Teuben, P. J. 1997, *ApJ*, 482, L143
- Richstone, D. O. 1998, in *IAU Symp. #186 Galaxy Interactions at Low and High Redshift*, in press
- Roberts, W. W. Jr., Huntley, J. M., & van Albada, G. D. 1979, *ApJ*, 233, 67
- Rots, A. 1980, *A&AS*, 41, 189
- Rowley, G. 1986, Ph.D. Thesis, The Australian National University
- Rowley, G. 1988, *ApJ*, 331, 124
- Rubin, V. C., Kenney, J. D. P., & Young, J. S. 1997, *AJ*, 113, 1250
- Sanders, D. B., & Mirabel, I. F. 1996, *ARAA*, 34, 749
- Sanders, R. H., & Tubbs, A. D. 1980, *ApJ*, 235, 803
- Schwarz, M. P. 1981, *ApJ*, 247, 77

- Sellwood, J. A., & Moore, E. M. 1999, *ApJ*, 510, 660
- Sellwood, J. A., & Wilkinson, A. 1993, *Rep. Prog. Phys.*, 56, 173
- Shaw, M. A. 1987, *MNRAS*, 229, 691
- Shaw, M. A., Axon, D., Probst, R., & Gatley, I. 1995, *MNRAS*, 274, 369
- Shaw, M. A., Wilkinson, A., & Carter, D. 1993, *A&A*, 268, 511
- Shlosman, I., Frank, J., & Begelman, M. C. 1989, *Nature*, 338, 45
- Sofue, Y. 1996, *ApJ*, 458, 120
- Sofue, Y., & Irwin, J. A. 1992, *PASJ*, 44, 353
- Staveley-Smith, L., Bland, J., Axon, D. J., Davies, R. D., & Sharples, R. M. 1990, *ApJ*, 364, 23
- Staveley-Smith, L., & Davies, R. 1988, *MNRAS*, 231, 833
- Stockton, A. 1998, in *IAU Symp. #186 Galaxy Interactions at Low and High Redshift*, in press
- Stone, J. L., Wilson, A. S., & Ward, M. J. 1988, *ApJ*, 330, 105
- Telesco, C. M., Dressel, L. L., Wolstencroft, R. D. 1993, *ApJ*, 414, 120
- Tully, R. B., Shaya, E. J., & Pierce, M. J. 1992, *ApJS*, 80, 479
- Veilleux, S., 1991, *ApJS*, 75, 357
- Veilleux, S., Bland-Hawthorn, J., Cecil, G., Tully, R. B., & Miller, S. T. 1999, *ApJ*, 520, 111 (VBCTM)
- Veilleux, S., Cecil, G., & Bland-Hawthorn, J. 1995, *ApJ*, 445, 152 (VCB)
- Veilleux, S., Cecil, G., Bland-Hawthorn, J., Tully, R. B., Filippenko, A. V., & Sargent, W. L. W. 1994, *ApJ*, 433, 48 (VCBTFS)
- Wada, K., & Habe, A. 1992, *MNRAS*, 258, 82
- Wainscoat, R. J., & Cowie, L. L. 1992, *AJ*, 103, 332
- Whittle, M., Pedlar, A., Meurs, E. J. A., Unger, S. W., Axon, D. J., & Ward, M. J. 1988, *ApJ*, 326, 125
- Wozniak, H., Friedli, D., Martinet, L., Martin, P., & Bratschi, P. 1995, *A&AS*, 111, 115
- Yasuda, N., Fukugita, M., & Okamura, S. 1997, *ApJS*, 108, 417
- Young, J. S., Claussen, M. J., & Scoville, N. Z. 1988, *ApJ*, 324, 115

Table 1: Fabry-Perot Observations

	NGC 3079	NGC 4388	NGC 4388
Emission Lines	H $\alpha$ + [N II] $\lambda\lambda$ 6548, 6583	H $\alpha$	[O III] $\lambda$ 5007
Dates of Observations	1990 March 14 – 17	1990 May 31 & June 1	1992 March 12
Total Exposure Time	20 hrs	6.3 hrs	7.0 hrs
Telescope	CFHT 3.6m	UH 2.2m	UH 2.2m
Field of View	4'6	10'	10'
Pixel Scale	0'57	0'66	0'85
Spectral Resolution	70 km s $^{-1}$	40 km s $^{-1}$	60 km s $^{-1}$
Number of Spectra	150,000	5,000	7,000



Table 2: Morphological and Kinematical Parameters of NGC 3079 and NGC 4388

Component	Parameter	NGC 3079	NGC 4388
Disk	$V_{\text{sys}}$	$1,150 \pm 25 \text{ km s}^{-1}$	$2,525 \pm 25 \text{ km s}^{-1}$
	$V_{\text{max}}$ (deprojected)	$250 \pm 25 \text{ km s}^{-1}$	$180 \pm 25 \text{ km s}^{-1}$
	P.A. (major axis)	$169^\circ \pm 4^\circ$	$90^\circ \pm 4^\circ$
	Inclination $i$	$82^\circ \pm 4^\circ$	$-78^\circ \pm 4^\circ$
	Scale length $R_s$	3.0 kpc	1.8 kpc
	Scale height $z_s$	0.38 kpc	0.32 kpc
	Adopted rotation curve	Smoothed version of observed rotation curve	Equation (3) with $V_0 = 180 \text{ km s}^{-1}$ and $\alpha = 0.1 \text{ arcsec}^{-1}$
Bulge	Axis ratio $a : b$	1:0.43	1:0.35
	Boxiness $p$	3.5	3.5
	Intensity relative to disk $I_{b0}/I_{d0}$	4.6	5.0
Bar	P.A. (intrinsic to disk)	$130^\circ \pm 10^\circ$	$135^\circ \pm 15^\circ$
	Inner radius $R_b$	3.6 kpc	1.5 kpc
	Orbit eccentricity $R \leq R_b$	0.7	0.3
	Angular velocity $\Omega_b = \Omega(R_b)$	$60 \text{ km s}^{-1} \text{ kpc}^{-1}$	$105 \text{ km s}^{-1} \text{ kpc}^{-1}$
	Outer radius $R_d$	6.0 kpc	5.1 kpc

Fig. 1.— Stellar morphology of NGC 3079. (a) K' band image of NGC 3079, (b) model consisting of an exponential disk and a box-shaped bulge, (c) model consisting of an exponential disk and a spherical bulge, (d) residuals resulting from the subtraction of (b) from (a).

Fig. 2.— The left panel shows the distribution of the H $\alpha$  emission in NGC 3079. The middle and right panels show the velocity fields derived from H $\alpha$  and [N II]  $\lambda$ 6583, respectively. Each panel shows the central  $125'' \times 280''$  ( $10.5 \text{ kpc} \times 23.5 \text{ kpc}$ ) of NGC 3079 with north at the top and east to the left. The line of nodes derived from each of these velocity fields is shown superposed as a series of black dots.

Fig. 3.— The top panel shows the rotation curve of NGC 3079 derived along the position of the line of nodes of the H $\alpha$  velocity field. The velocity range at each radius represents  $\pm 1 \sigma$ . The full line is the smoothed, flux-weighted rotation curve used in the two-dimensional fits to the velocity field (Fig. 4). The dashed line corresponds to the systemic velocity,  $1,150 \text{ km s}^{-1}$ . The velocities along the minor axis are shown in the lower panel.

Fig. 4.— Predicted velocity fields for (a) an axisymmetric disk, (b) a disk with bar streaming motions. The residual maps (observed H $\alpha$  velocity field of NGC 3079 – model) for the axisymmetric and bar models are presented in panels (c) and (d), respectively. The parameters of the bar model are listed in Table 2. The bar model fits the central disk considerably better.

Fig. 5.— Stellar morphology of NGC 4388. (a) H-band image of NGC 4388, (b) model consisting of an exponential disk and a box-shaped bulge, (c) model consisting of an exponential disk and a spherical bulge, (d) residuals resulting from the subtraction of (b) from (a).

Fig. 6.— Velocity field of the line-emitting gas in NGC 4388. (top) [O II]  $\lambda$ 5007; (bottom) H $\alpha$ . North is at the top and east to the left.

Fig. 7.— Rotation curve of NGC 4388. The data points were derived along the position of the line of nodes of the H $\alpha$  velocity field. The rotation curve was stopped where outflowing motions north-east of the nucleus become significant. The dotted line shows the systemic velocity of the galaxy,  $2,525 \text{ km s}^{-1}$ . The solid lines represent two attempts to fit these data using equation (3). The thin solid line uses  $V_0 = 120 \text{ km s}^{-1}$  and  $\alpha = 0.18 \text{ arcsec}^{-1}$  while the thick line uses  $V_0 = 180 \text{ km s}^{-1}$  and  $\alpha = 0.10 \text{ arcsec}^{-1}$ . The two-dimensional bar model subtraction shown in Figure 8d clearly demonstrates that the rotation curve represented by the thick line is a better representation of the data. The deviations from the modeled rotation curve are due to streaming motions.

Fig. 8.— Predicted velocity fields for (a) an axisymmetric disk, (b) a disk with bar streaming motions. The residual maps (observed H $\alpha$  velocity field of NGC 4388 – model) for the axisymmetric and barred disk models are presented in panels (c) and (d), respectively. The parameters of the barred disk model are listed in Table 2. The barred disk model fits the observations considerably better.

Fig. 9.— The top panel shows the deprojected rotation curve used in our fit of the Fabry-Perot data of NGC 3079 with a bar model (solid line in the top panel of Figure 3) and the best-fit rotation curve calculated using a Freeman exponential disk (dashed curve) and an isothermal dark halo (dotted line). See text for detail. The lower panel shows the behavior of  $\Omega$  (thick solid line),  $\Omega \pm \kappa/2$  (dotted lines) and  $\Omega_b$  (dashed line) derived using the best-fit rotation curve in the upper panel. No ILR appears to be present in NGC 3079.

Fig. 10.— Same as Figure 9 but for NGC 4388. The best-fit rotation curve from Figure 7 (the thick solid line in that figure) was used for the calculations after deprojection. No ILR appears to be present in NGC 4388.

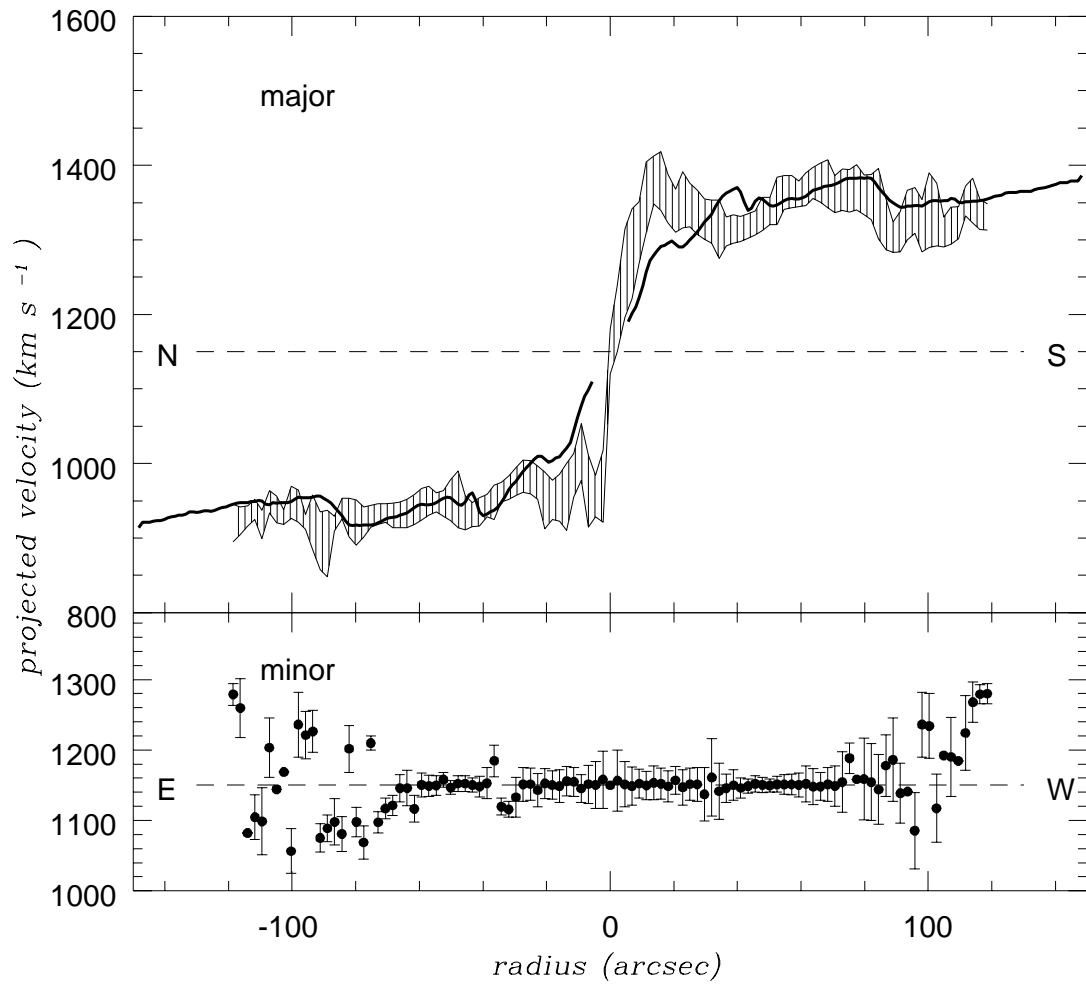


Fig. 3.—

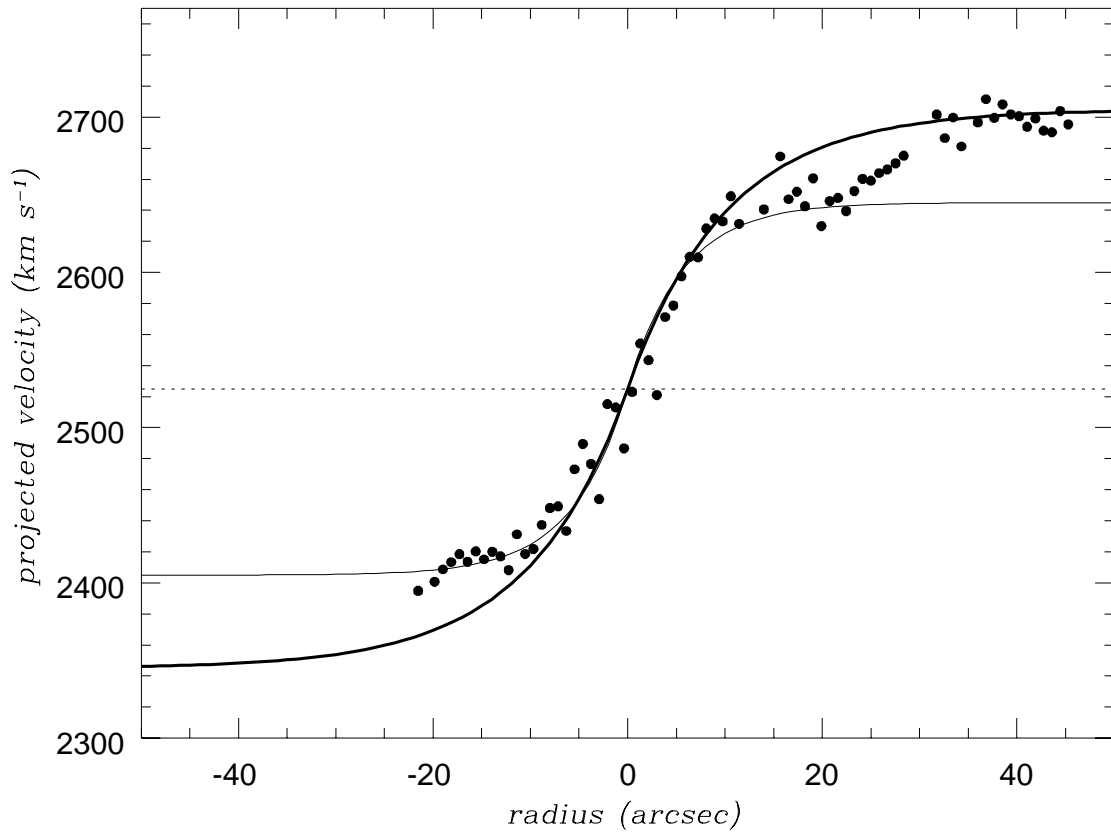


Fig. 7.—

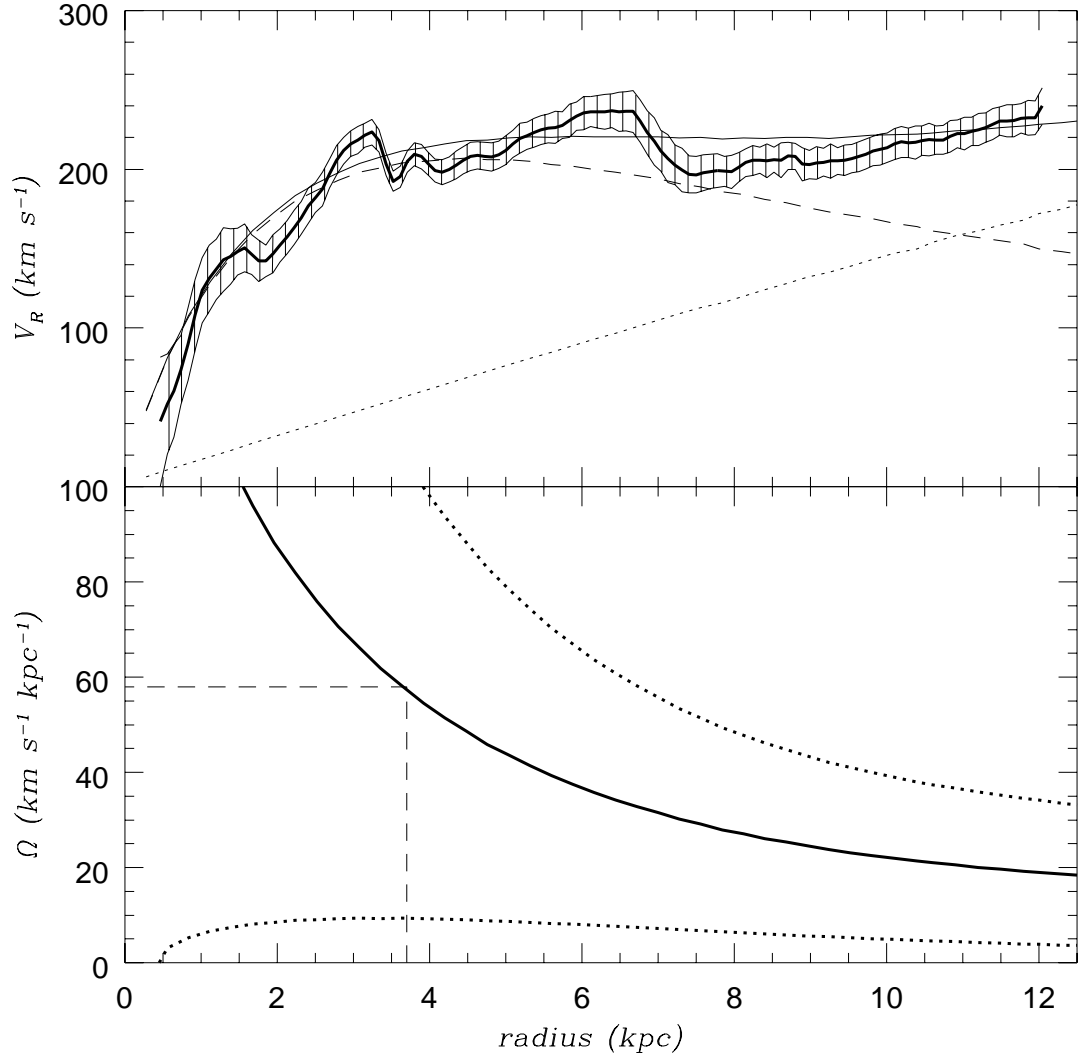


Fig. 9.—

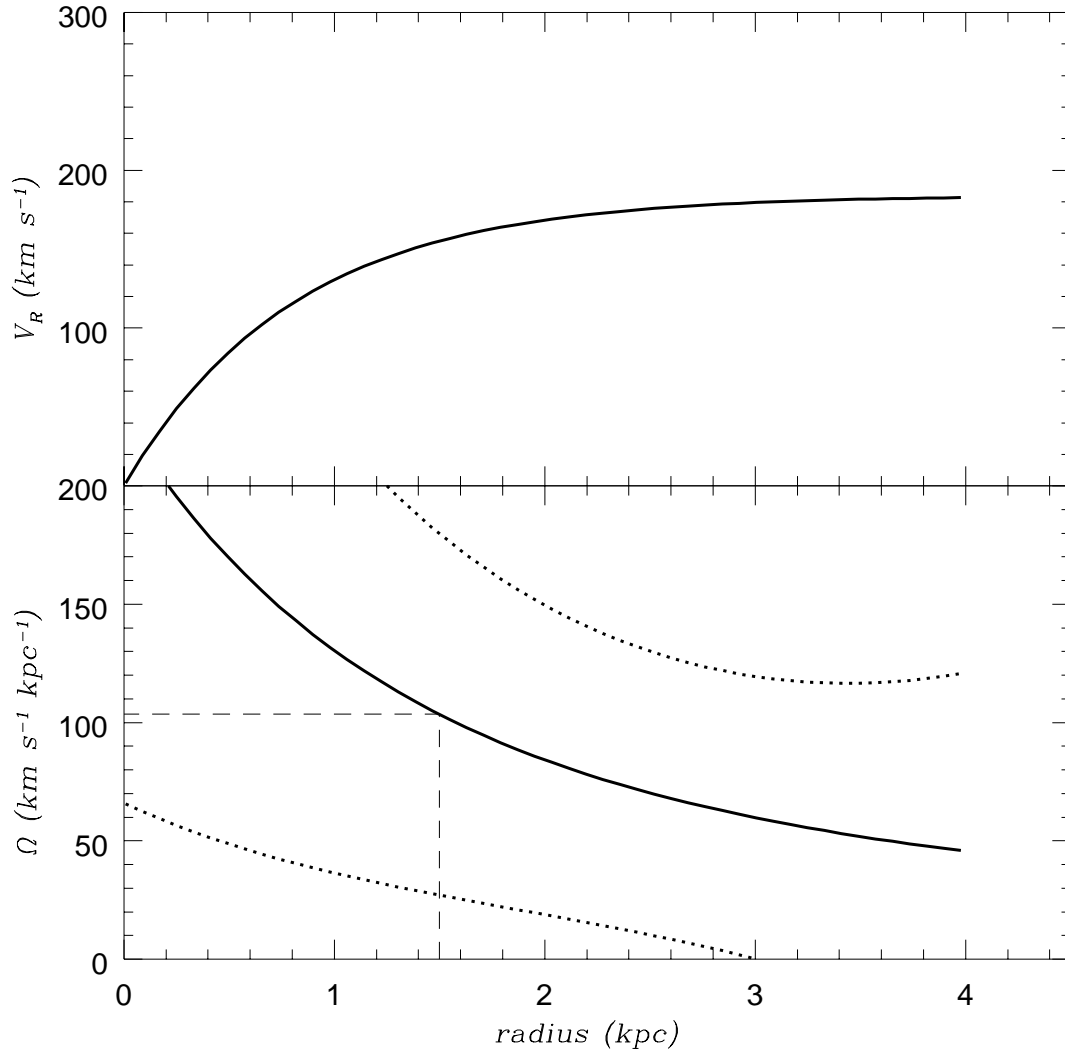


Fig. 10.—

This figure "Fig1.gif" is available in "gif" format from:

<http://arxiv.org/ps/astro-ph/9907444v1>



This figure "Fig2a.gif" is available in "gif" format from:

<http://arxiv.org/ps/astro-ph/9907444v1>

This figure "Fig2b.gif" is available in "gif" format from:

<http://arxiv.org/ps/astro-ph/9907444v1>

This figure "Fig2c.gif" is available in "gif" format from:

<http://arxiv.org/ps/astro-ph/9907444v1>

This figure "Fig4a.gif" is available in "gif" format from:

<http://arxiv.org/ps/astro-ph/9907444v1>

This figure "Fig4b.gif" is available in "gif" format from:

<http://arxiv.org/ps/astro-ph/9907444v1>

This figure "Fig4c.gif" is available in "gif" format from:

<http://arxiv.org/ps/astro-ph/9907444v1>

This figure "Fig4d.gif" is available in "gif" format from:

<http://arxiv.org/ps/astro-ph/9907444v1>

This figure "Fig5.gif" is available in "gif" format from:

<http://arxiv.org/ps/astro-ph/9907444v1>



This figure "Fig6.gif" is available in "gif" format from:

<http://arxiv.org/ps/astro-ph/9907444v1>

This figure "Fig8a.gif" is available in "gif" format from:

<http://arxiv.org/ps/astro-ph/9907444v1>

This figure "Fig8b.gif" is available in "gif" format from:

<http://arxiv.org/ps/astro-ph/9907444v1>

This figure "Fig8c.gif" is available in "gif" format from:

<http://arxiv.org/ps/astro-ph/9907444v1>

This figure "Fig8d.gif" is available in "gif" format from:

<http://arxiv.org/ps/astro-ph/9907444v1>